Available online at www.sciencedirect.com

SciVerse ScienceDirect

Acta Materialia 61 (2013) 5504–5517

Acta MATERIALIA

www.elsevier.com/locate/actamat

Interaction between recrystallization and phase transformation during intercritical annealing in a cold-rolled dual-phase steel: A cellular automaton model

Chengwu Zheng [a,b,*], Dierk Raabe [b,*]

[a] Institute of Metal Research, Chinese Academy of Sciences, Wenhua Road 72, Shenyang 110016, China
[b] Max-Planck Institut für Eisenforschung, Max-Planck-Straße 1, Düsseldorf 40237, Germany

Received 13 December 2012; received in revised form 30 May 2013; accepted 30 May 2013
Available online 24 June 2013

Abstract

The concurrent ferrite recrystallization and austenitic transformation during intercritical annealing of cold-rolled DP steels is investigated by cellular automaton (CA) modeling. The simulations provide insight into the microstructural phenomena that result from the interaction of primary recrystallization and phase transformation. We find that the interaction between ferrite recrystallization and austenite formation affects not only the transformation kinetics but also the morphology and spatial distribution of the austenite. From this we can interpret experimental data of the observed temperature-dependent hardness and its dependence on the two metallurgical processes. The influence of the initial heating rate on subsequent isothermal transformation kinetics and the microstructure evolution is also obtained by the model.

Keywords: Intercritical annealing; Ferrite recrystallization; Austenitization; Cellular automaton; Mesoscopic modeling

1. Introduction

Owing to a favorable combination of high strength and good formability, dual-phase (DP) steels are currently receiving high interest in the automotive industry for low energy consumption vehicle design through weight reduction [1–6]. The microstructure of DP steel is characterized by hard martensite islands dispersed in a soft and ductile ferrite matrix [7]. To generate DP microstructures, a continuous annealing process that includes reheating of a cold-rolled ferrite/pearlite microstructure followed by intercritical annealing is implemented to form an austenite/ferrite mixture, which after final quenching results in a DP microstructure [8]. During this process, microstructure formation is determined by a number of interacting metallurgical phenomena, of which ferrite recrystallization, austenite formation and carbon diffusion are the most important. What makes the prediction of DP microstructures challenging is the fact that these phenomena may proceed consecutively or simultaneously, i.e. complex local interactions between the metallurgical diffusion and transformation phenomena occur. The nonlinear character of the phenomena involved minor changes in these interactions, and this may have a profound influence on the resulting microstructure. On the other hand, from a theoretical point of view, it is also an essential challenge to quantitatively understand and evaluate the interdependence and competition between these two metallurgical processes.

In earlier studies, such potential interactions between recrystallization and phase transformation have been reported to occur for various intercritically annealed steels on materials that had been initially cold rolled [9–11]. Yang

* Corresponding authors. Address: Institute of Metal Research, Chinese Academy of Sciences, Wenhua Road 72, Shenyang 110016, China. Tel.: +86 24 83970106; fax: +86 24 83970097 (C. Zheng), tel.: +49 211 6792 340; fax: +49 211 6792 333 (D. Raabe).
E-mail addresses: chwzheng@hotmail.com (C. Zheng), d.raabe@mpie.de (D. Raabe).

1359-6454/$36.00
http://dx.doi.org/10.1016/j.actamat.2013.05.040

et al. [9] observed austenite nucleation both on grain boundaries of unrecrystallized ferrite and at the interfaces between recrystallized and unrecrystallized grains. This work revealed an influence of ferrite recrystallization on the formation and distribution of austenite. Huang et al. [10] systematically investigated the effect of the initial heating rate on austenite formation and ferrite recrystallization in two steels with chemical compositions that are typically used for DP and transformation-induced plasticity (TRIP) steels. They suggested that there was a strong interaction between ferrite recrystallization and austenite formation, which could affect the kinetics of austenite formation as well as its spatial distribution. Their findings were recently verified by Azizi-Alizamini et al. [11] in a plain low-carbon steel, including a similar morphology shift from randomly distributed to a banded structure of austenite when increasing the initial heating rate. Despite these important findings and their potential practical relevance, further investigations of such interaction phenomena as well as their potential effect on the final microstructure and properties of the steels annealed in the intercritical region are still required. More specifically, the interaction between the two metallurgical processes may cause property variations and makes it difficult to identify the relation between direct thermal processing settings and the final product properties. However, the approach of integrated microstructural simulation that includes all relevant metallurgical processes is ideally suited to provide the desired insight for this problem, which hence enables us to conduct quantitative microstructure design for optimal properties.

With the recent development of mesoscale microstructure-based transformation models [12], e.g. the cellular automaton (CA), the Monte Carlo (MC) and the phase field (PF), simulations can now provide deeper insight into the mechanism and morphological complexity of both the phase transformation and recrystallization in steels [13,14]. Numerical modeling is thus emerging as an alternative tool to investigate the interaction mechanism of recrystallization and phase transformation in DP steels. Recently, Rudnizki et al. [15] developed a PF model to describe the austenite formation from a ferrite–pearlite aggregate during the annealing of a cold-rolled DP steel. However, their simulation started from an already recrystallized microstructure. Hence, the approach did not consider the interaction between recrystallization and phase transformation. Bos et al. [16,17] presented an integrated three-dimensional (3-D) CA model to describe the through-process microstructure evolution during the entire processing of DP steels. In their model, simulation of concurrent ferrite recrystallization and austenite formation was involved. However, their interest was placed on the model development [16] and its usage on a study of the influence of individual transformation processes on the final DP microstructure [17], whereas the interaction between recrystallization and phase transformation was not addressed. Okuda et al. [18] performed an MC simulation to examine the competition between recrystallization and transformation in several DP microstructures. However, their model did not involve detailed thermodynamic criteria of either recrystallization or phase transformation.

In this work, we present a modified two-dimensional (2-D) CA model to investigate the competition between ferrite recrystallization and austenitic transformation during the intercritical annealing of cold-rolled DP steels. In this model, discrete microstructural constituents either in recrystallization or in phase transformation are depicted through involving relevant thermodynamic criteria (stored deformation energy, chemical transformation driving force, etc.) and kinetic effects (grain boundary mobility, carbon diffusion, etc.), so that a detailed microstructural insight into the mutual interactions between these various metallurgical processes can be obtained. This model also enables us to study the influence of initial heating rate and annealing temperature on subsequent isothermal transformation kinetics and the associated microstructure evolution.

2. Model concept

2.1. Austenite transformation

During the intercritical annealing of DP steels, two different situations of austenite nucleation are usually considered [19,20]. One is related to the austenite formation at the ferrite/cementite interfaces within the carbon containing colonies, e.g. within the pearlite. The other is the nucleation on the ferrite/ferrite grain boundaries. In general, nucleation of austenite starts from the pearlite colonies. The newly formed austenite nuclei grow rapidly at the expense of the pearlite and subsequently of the ferrite. During this process, austenite growth is mainly limited by carbon diffusion inside the austenite, as schematically represented in Fig. 1. The transformation proceeds much faster for the pearlite-nucleated austenite than that in ferrite due to the

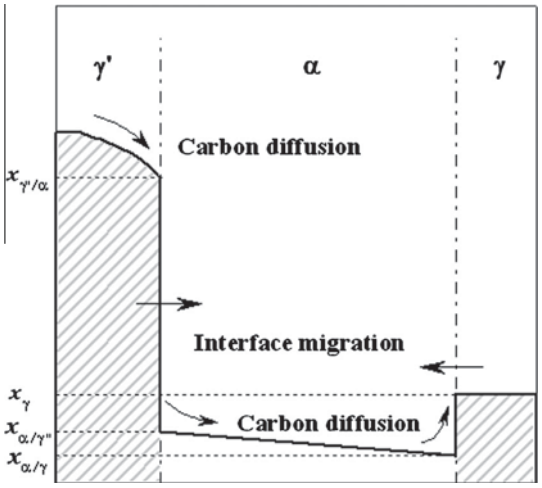

Fig. 1. Schematic drawing about the variation in the carbon content across the austenite–ferrite boundary [20]: γ' = pearlite-nucleated austenite, α = ferrite and γ = grain-boundary-nucleated austenite.

available surplus of carbon. As for the austenite nucleation at the ferrite/ferrite boundaries, an austenite nucleus forms without direct contact with the carbon source. In this case, the subsequent growth of the austenite nuclei requires carbon diffusion from the carbon-rich areas through the ferrite matrix in order to support the austenite formation at the moving γ/α interface, as shown in Fig. 1.

In our current simulation, both scenarios of austenite nucleation, namely nucleation within pearlite and nucleation on ferrite/ferrite boundaries, are considered. The austenite nucleated within the carbon-rich regions is here referred to as "pearlite-nucleated austenite" and that formed at the ferrite grain boundaries as "grain-boundary-nucleated austenite".

In order to describe the two situations of austenite formation, a mixed-mode growth kinetics model [21] is adopted in the present simulations. The interface velocity can be described by [22]

$$v_{\alpha\gamma} = M^{\alpha\gamma}\Delta G \tag{1}$$

where $M^{\alpha\gamma}$ is the interface mobility and ΔG is the chemical driving force. The mobility is assumed to follow an Arrhenius relationship [23]:

$$M^{\alpha\gamma} = M_0^{\alpha\gamma}\exp\left(-Q_{\alpha\gamma}/RT\right) \tag{2}$$

where $Q_{\alpha\gamma}$ is the activation energy for boundary migration, $M_0^{\alpha\gamma}$ is the pre-exponential factor of the interface mobility, and R and T are the universal gas constant (8.314 J mol^{-1} K^{-1}) and absolute temperature, respectively.

The chemical driving force, ΔG, is here considered in a first approximation as proportional to the deviation from the equilibrium concentration on the moving interface [24,25]. For the austenite formed within the pearlite colonies, the driving force for growth outwards into ferrite can be rewritten as [24,25]

$$\Delta G_{\mathrm{I}} = \chi_{(T)}\left(x^{\gamma'/\alpha} - x^{\gamma}\right) \tag{3}$$

where $\chi_{(T)}$ is a proportionality factor, which can be calculated using Thermo-Calc [26]. $x^{\gamma'/\alpha}$ and x^{γ} are the carbon concentrations at the moving γ/α interface and the equilibrium concentration of austenite, respectively, as shown in Fig. 1. In the current simulation, pearlite is treated as a single effective phase with an averaged carbon content of 0.71 wt.% (i.e. the eutectoid carbon concentration for this specific alloy).

As for the austenite nucleated at the ferrite grain boundaries, the driving force for the austenite growth can be described by

$$\Delta G_{\mathrm{II}} = \chi_{(T)}\left(x^{\alpha/\gamma} - x^{\alpha}\right) \tag{4}$$

with $x^{a/\gamma}$ the interfacial carbon concentration at the ferrite side of the moving interface and x^{α} the equilibrium ferrite concentration at the given temperature. x^{γ} and x^{α} can be derived from the Fe–C phase diagram.

The solute diffusion in the two phases (α and γ) is described by

$$\frac{\partial x_c^{\phi}}{\partial t} = \nabla\cdot\left(D_c^{\phi}\nabla x_c^{\phi}\right) \tag{5}$$

where ϕ acts as a structure indicator and denotes either phase α or phase γ, x_c^{ϕ} is the carbon concentration in phase ϕ and D_c^{ϕ} is the carbon diffusion coefficient in either the α or γ phase. The diffusion coefficient D_c^{ϕ} is assumed to be thermally activated according to

$$D_c^{\phi} = D_{c,0}^{\phi}\exp\left(-Q_c^{\phi}/RT\right) \tag{6}$$

with $D_{c,0}^{\phi}$ the pre-exponential constant and Q_c^{ϕ} the activation energy for carbon diffusion.

In this simulation, austenite nucleation is described as a continuous nucleation event. The dependence of nucleation rate $\dot{N}_A$ on the annealing temperature is described according to the classic nucleation theory [27]:

$$\dot{N}_A = K_1 D_c^{\gamma}(kT)^{-\frac{1}{2}}\exp\left(-\frac{K_2}{kT(\Delta G_N)^2}\right) \tag{7}$$

where K_1 is a constant related to the nucleation site density, K_2 is a constant related to all the interface involved in nucleation, D_c^{γ} is the carbon diffusion coefficient in austenite, k is the Boltzmann constant (1.38×10^{-23} J K^{-1}) and ΔG_N is the driving force for austenite formation. The driving force ΔG_N depends on the annealing temperature and the carbon concentration, i.e. the carbon concentration of the initial pearlite and the ferrite. Then the nucleation rate of the two austenite nucleation scenarios can be distinguished. ΔG_N is here also considered to be proportional to the deviation from the equilibrium concentration as indicate by Eqs. (3) and (4).

2.2. Ferrite recrystallization

Nucleation of primary static recrystallization is treated as a thermally activated process. We implemented a continuous nucleation law to describe ferrite recrystallization. The nucleation rate $\dot{N}_{RX}$ is described by a phenomenological relation [28]:

$$\dot{N}_{RX} = C_0\left(E_D - E_D^C\right)\exp\left(-Q_{RX}^N/RT\right) \tag{8}$$

with E_D the stored deformation energy, E_D^C the critical stored deformation energy for triggering recrystallization which can be determined by the critical deformation strain and Q_{RX}^N the apparent activation energy for ferrite recrystallization. C_0 is a fitting parameter (1.7×10^{14} s^{-1} J^{-1}). Here, E_D^C is set as the stored deformation energy at the strain of 0.1. Recrystallization nucleation is hence treated as being both temperature- and time-dependent.

The velocity of the recrystallization front, v_{RX}, moving into the deformed ferrite can be expressed as follows [29]:

$$v_{RX} = M^{RX}(E_D - P_Z) \tag{9}$$

where E_D is the driving pressure for the primary static recrystallization front movement, which is provided by the difference in stored deformation energy between the recrystallized grains and the deformed matrix, and P_Z is

the potential pinning force stemming from the precipitation of small austenite particles [30]. The stored deformation energy, E_D, is related to the dislocation density, ρ:

$$E_D = \frac{1}{2}\mu b^2 \rho \tag{10}$$

where μ is the shear modulus of the material and ρ is a function of the prior strain level and the deformation temperature. During the continuous annealing of cold-rolled DP steels, the stored deformation energy will be released due to recovery. The evolution of the stored energy $E_D(t)$ as function of temperature T and annealing time t is given as follows [31]:

$$E_D(t) = \left[E_D(t_0)^{1/2} - C_1 \mu^{-1/2} kT \ln\left(1 + \frac{t}{\tau_0}\right)\right]^2 \tag{11}$$

where $E_D(t_0)$ is the initial stored energy of deformation, t_0 is the time when recovery starts, C_1 is a combined fitting parameter ($5.7 \times 10^{18}\ \mathrm{m}^{-3}$), μ is the shear modulus of the material and k and T have their usual meanings. Recovery is assumed to occur from the start of the reheating process, i.e. $t_0 = 0$ s. τ_0 is a time constant which is set as 1 s in this simulation. Details of the calculation of the stored deformation energy can be found in Refs. [32,33].

The Zener-based particle back-driving force derived from small-sized austenitic precipitations, P_Z, can be described by [34]

$$P_z = \frac{3}{2}\gamma_m \frac{f_p}{r} \tag{12}$$

here γ_m is the grain boundary energy, f_p is the volume fraction of the grain boundary nucleated austenite particles and r is their mean radius. M^{RX} is the boundary mobility of high angle grain boundary which can be estimated by [35]

$$M^{RX} = \frac{D_0 b^2}{kT} \exp\left(-\frac{Q_b}{RT}\right) \tag{13}$$

where Q_b is the activation energy for grain-boundary motion, D_0 is the boundary self-diffusion coefficient and b is the magnitude of the Burgers vector.

2.3. Grain coarsening

Competitive growth of the grains caused by the boundary curvature effect would lead to grain coarsening after hard impingement among the neighboring grains. The velocity of a grain boundary segment driven by the curvature can be expressed by [36]

$$v_{\gamma\gamma} = M^{\gamma\gamma} F \tag{14}$$

where $M^{\gamma\gamma}$ is the grain boundary mobility between grains and F is the driving force originating from interface curvature. The driving force for capillary-driven grain boundary motion F is expressed by [36]

$$F = \eta\kappa \tag{15}$$

where η is the grain boundary energy and κ is the curvature of the grain boundary. In the present model, the grain boundary curvature is calculated using an approach known from the curvature calculation in lattice-based models [37]:

$$\kappa = \frac{A}{C_{cell}} \frac{Kink - N_i}{N + 1} \tag{16}$$

where C_{cell} is the grid spacing in the CA model, $A = 1.28$ is a topological coefficient, $N = 18$ is the number of the first and second nearest neighbor sites for a hexagonal lattice, N_i is the number of cells within the neighborhood belonging to grain i and $Kink = 9$ is the number of cells within the neighborhood belonging to grain i for a flat interface ($\kappa = 0$). The topological considerations behind this model can be found in Figs. A1–A3 in Ref. [37].

3. CA model

In this work, a 2-D CA approach is implemented as a solver to simulate the competing phase transformation and the recrystallization phenomena in a DP steel according to the equations outlined above. In this formulation, the spatial system is discretized onto a 2-D regular equal spaced hexagonal lattice. Each cell represents a volume of real material characterized by certain attributes with a distinct phase, solute content and an orientation indictor. The neighbors of a cell are defined by von Neumann's rule, which considers the nearest six cells. In order to describe the microstructure evolution of phase transformation and recrystallization during the intercritical annealing, eight state variables are used on each CA node. These are: (1) the phase state variable that denotes whether the cell is pearlitic, ferritic, austenitic or contains γ/α, P/γ interfaces; (2) the ferrite recrystallization status that indicates whether it belongs to deformed ferrite, recrystallized ferrite or the interface; (3) the carbon concentration variable; (4) the orientation variable which is assigned an integer identifier representing its crystallographic orientation; (5) the austenite transformation fraction variable, f_γ, quantifying the austenite fraction transformed from ferrite; (6) the austenite transformation fraction variable, f'_γ, representing the austenite fraction transformed from pearlite; (7) the ferrite recrystallization fraction variable, f_{RX}; and (8) the fraction variable, f, used for the motion of the boundary segment within an γ/γ or α/α boundary cell.

The values of each state variable on each of the CA nodes are functions of their respective previous states and the previous states of their neighbors. They are determined according to the sub-models described in Section 2. The kinetics of the automaton is realized by synchronously updating the state variables for all lattice cells in each time step.

Details regarding the mapping of the constitutive and kinetic laws outlined above into the discrete CA approach, i.e. nucleation, growth and competitive grain coarsening for phase transformation and recrystallization, are given

in Refs. [38,39]. Here, only the items relevant to the current simulation are outlined in more detail:

(1) The grid size used in the present CA model is 0.4 μm, which is too coarse to describe the individual pearlitic lamellae structure. Pearlite is hence considered as one effective phase with a carbon concentration of 0.71 wt.% in accordance with a Thermo-Calc calculation.
(2) The growth of austenite into pearlite is assumed to be controlled solely by interface migration, with the driving force derived from the effective pearlite carbon concentration (0.71 wt.%).
(3) Simulation of cementite spheroidization/dissolution and the associated effects on the carbon concentration field and subsequent austenite formation are not involved.
(4) A contribution of the stored deformation energy as an additional portion to the driving force for phase transformation is not considered. This means that the occurrence of primary recrystallization does not alter the (chemical) driving force for phase transformation.
(5) Curvature-driven grain coarsening is assumed to occur between austenite grains as well as with recrystallized ferrite grains after impingement.

4. Microstructure set-up and initial conditions

The simulated material is a DP steel with chemical composition (wt.%) 0.08 C, 0.01 Si and 1.75 Mn. The transformation temperature A3 is calculated as 817 °C by Thermo-Calc. In order to create the starting microstructure for the simulation, a method indicated by Bos et al. [16] has been implemented. A fine, unbanded ferrite–pearlite aggregate is firstly built using a separate CA simulation, as shown in Fig. 2a. The white regions indicate ferrite and the gray areas are pearlite colonies. The black lines represent the α/α grain boundaries or α/P hetero-interfaces. The initial simulated domain is defined by a 150×700 CA lattice, representing a physical domain of 60 μm × 280 μm in real material. The initial structure consists of ~9 vol.% pearlite and 91 vol.% ferrite. The initial average ferrite grain size (diameter) is ~15 μm. In this simulation, pearlite is considered as one effective phase, as assumed in previous simulations [15–17], with an effective carbon concentration of 0.71 wt.%. The ferrite matrix is assigned an initial carbon concentration of 0.01 wt.% [40]. Then a uniaxial compression of 80% thickness reduction is applied to mimic a cold-rolled grain structure (Fig. 2b). The simulated domain is correspondingly mapped onto a 498×210 CA lattice, equivalent to 199 μm × 84 μm in the real material. The microstructure is characterized by the alignment of ferrite and pearlite along the rolling direction. This specific cold-rolling microstructure is important for the subsequent topology evolution during ferrite recrystallization. Firstly, the distribution and shape of the pearlite colonies are geometrically modified by the simulated cold deformation. This type of distorted microstructure provides characteristic boundary conditions for the grain growth during ferrite recrystallization. Secondly, the prior cold deformation in the mixed-microstructure with hard pearlite and soft ferrite introduces an inhomogeneous distribution of the deformation energy. The stored deformation energy is concentrated in the vicinity of the pearlite/ferrite boundaries which, therefore, provide favorable sites for the nucleation of ferrite recrystallization. In the current simulation, both the ferrite/ferrite grain boundaries and the pearlite/ferrite interfaces are hence defined as preferential nucleation sites for ferrite recrystallization.

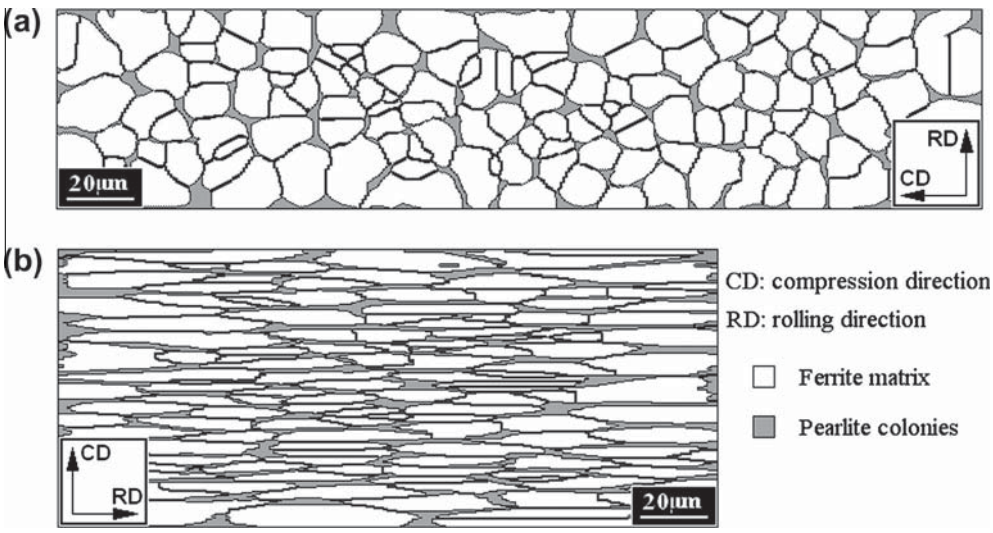

Fig. 2. Formation of the starting microstructure for the intercritical annealing simulation: (a) the initial unbanded ferrite–pearlite aggregate before deformation; (b) the microstructure after 80% cold reduction as input for the simulation. In this model, pearlite is treated as a single effective phase.

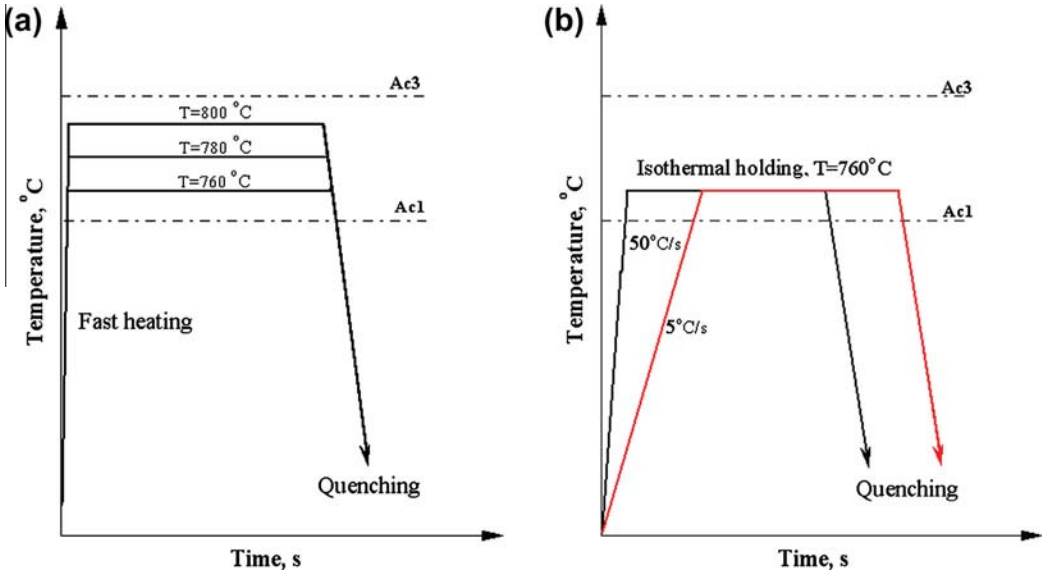

Fig. 3. Schematic representation of the thermal cycles used in current simulations: (a) influence of various intercritical temperatures; a fast reheating is imposed here; (b) influence of the initial heating rate.

The related thermal processing schedule implemented in the simulation is shown schematically in Fig. 3. To study the interaction between ferrite recrystallization and austenite formation under isothermal conditions, fast heating is imposed to yield full coupling between these two processes during the isothermal annealing. Then the influence of various intercritical temperatures is discussed, as shown in Fig. 3a. As for the heating rate examination, two specific rates of 50 and 5 °C s^{-1} are applied, where the samples are heated into the intercritical region at the two heating rates (50 and 5 °C s^{-1}) and then held for a predetermined time at the given annealing temperature, as seen in Fig. 3b. The key parameters used in the modeling are listed in Table 1.

5. Simulation results and discussion

5.1. Interaction between ferrite recrystallization and austenite transformation during intercritical annealing

During intercritical annealing of the cold-rolled DP steel, competition and overlap of ferrite recrystallization and austenite transformation takes place. For a better understanding of the interactions between these two phenomena, we here consider in more detail isothermal annealing at an intercritial temperature of 760 °C where full coupling of these two processes occurs. Fig. 4 shows the simulated transformation kinetics of competitive ferrite recrystallization and austenite formation at 760 °C. The associated kinetics of microstructure formation (left-hand side) and the carbon concentration fields in the ferrite (right-hand side) are shown in Fig. 5. In the simulated microstructures, the yellow regions indicate the austenite formed within the original pearlite domains (γ'). The small red patches are the austenite grains formed at ferrite grain boundaries (γ). The blue areas are the recrystallized ferrite (α_R), and the white zones are the non-recrystallized ferrite (α_{NR}).

During intercritical annealing, austenite formation starts from the initial pearlite colonies by nucleation, occurring instantaneously [4]. Subsequently, these austenite nuclei grow rapidly, consuming the dissolving pearlite until the original pearlite is replaced entirely. However, the morphology of the newly formed austenite grains is strongly

Table 1
The parameters used in simulations.

Symbol	Definition and unites	Value	Refs.
K_1	Austenite nucleation factor ($J^{1/2}\,m^{-4}$)	2.07×10^{11}	[27]
K_2	Austenite nucleation factor ($J^3\,m^{-2}$)	2.5×10^{-18}	[41]
D_c^{γ}	Carbon diffusion coefficient in austenite ($m^2\,s^{-1}$)	$1.5 \times 10^{-5}\exp(-142{,}100/RT)$	[42]
D_c^{α}	Carbon diffusion coefficient in ferrite ($m^2\,s^{-1}$)	$2.2 \times 10^{-4}\exp(-122{,}500/RT)$	[42]
$M^{\alpha\gamma}$	Mobility of the α/γ interface (mol m $J^{-1}\,s^{-1}$)	$0.5\exp(-140{,}000/RT)$	[21,32]
M^{RX}	Mobility of high angle α/α grain boundary ($m^4\,J^{-1}\,s^{-1}$)	$\frac{0.429}{T}\exp(-120{,}000/RT)$	[32]
Q_{RX}^N	Activation energy for ferrite recrystallization (kJ mol^{-1})	170	[33]
b	Burgers vector (m)	2.58×10^{-10}	[32]
γ_m	Grain boundary energy of high-angle α/α boundary ($J\,m^{-2}$)	0.56	[32]
u	Shear modulus of ferrite (GPa)	32	[32]

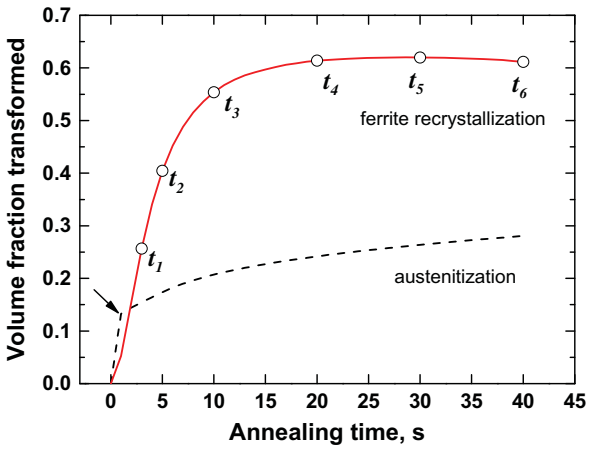

Fig. 4. Kinetics of ferrite recrystallization and austenite formation in the cold-rolled DP steel intercritically annealed at 760 °C. Here, a fast initial heating rate is imposed.

determined by the shape of the initial pearlite zones, which hence produces banding structures of austenite, as revealed in Fig. 5. Such austenite bands lead to local growth conditions such as encountered in thin films for the concurrent ferrite recrystallization. Therefore, further growth of recrystallizing ferrite grains along the compression direction will be topologically restricted. This effect results in a slow recrystallization rate [43]. Moreover, with the recrystallization front traversing across the region between the closely spaced austenite colonies, the strongly curved moving boundaries would experience pinning at the interfaces in conjunction with different constituents, which also slows down the recrystallization rate.

The pearlite-nucleated austenite forms with relatively high carbon concentrations, which leads to high driving forces acting on the α/γ' interfaces moving to sweep the surrounding ferrite. Therefore, rapid thickening and lengthening of the austenite bands is expected at the beginning of the α-to-γ' dissolution. Advancing of rapid austenite thickening affects the concurrent ferrite recrystallization as follows: (I) if the surrounding ferrite matrix remains unrecrystallized, rapid thickening of the austenite bands will consume most of the potential nucleation sites of recrystallization located in the vicinity of prior α/P interfaces. As a consequence, nucleation of ferrite recrystallization will be inhibited through the elimination of its most favorable interface nucleation sites by the advancing austenite interfaces. This effect can be clearly observed in the simulated microstructure in Fig. 5c. We can see that a considerable amount of ferrite still remains un-recrystallized, even after a long period of annealing up to 40 s. In these regions, further nucleation of recrystallization is blocked

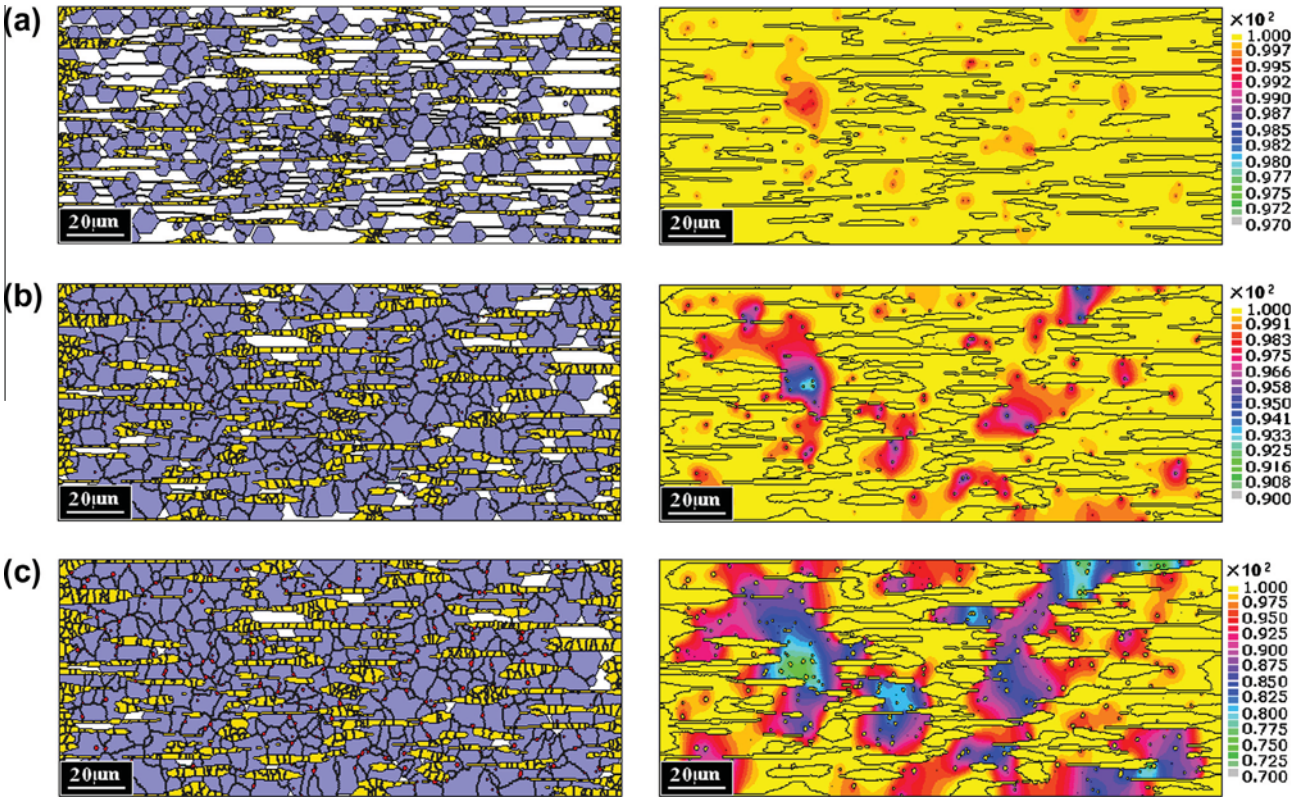

Fig. 5. Simulated microstructure (left) and the carbon concentration field (wt.%) in ferrite phase (right) at different soaking times as indicated in Fig. 4: (a) $t_2 = 5$ s, (b) $t_4 = 20$ s; (c) $t_6 = 40$ s during the isothermal holding of 760 °C. In the simulated microstructure (image left-hand side), the yellow areas are the pearlite-nucleated austenite; the small-sized red patches (image left-hand side) are the grain-boundary-nucleated austenite. The blue regions indicate the recrystallized ferrite and the white indicate unrecrystallized ferrite (image left-hand side). The black lines in the figures indicate the grain boundaries. The images on the right-hand side indicate the distribution of carbon. (For interpretation of the references to color in this figure legend, the reader is referred to the web version of this article.)

completely. The recrystallization becomes dominated solely by growing laterally into the deformed matrix. However, the well-recovered microstructure produces extremely low driving forces for the migration of the recrystallization fronts, which is responsible for the prevalence of the residual deformed ferrite. (II) If the surrounding ferrite has already been recrystallized, the intensive austenite growth will occupy the recrystallized regions and transform them into austenite. The recrystallization fraction hence is decreased gradually due to the phase transformation. This will lead to a competition of recrystallization softening and phase transformation hardening in the material properties as discussed in Section 5.2.

During intercritical annealing, austenite nuclei may also appear at various ferrite grain boundaries, i.e. the α_R/α_R, α_R/α_{NR} or α_{NR}/α_{NR} boundaries. Savran et al. [19] once provided a thermodynamic explanation on the austenite formation within the intercritical temperature range. They argued that beyond the preferable austenite formation in the carbon-rich areas, such as pearlite, nucleation is also possible at lower than equilibrium carbon content in austenite, which can favor nucleation on the boundaries of ferrite grains without contact with cementite [19]. In this case, as indicated in Fig. 1, the austenite formation is promoted by the carbon rejected from the ferrite-solid solution. However, subsequent growth of these austenite grains highly depends on the carbon removal from the carbon-rich area towards the moving γ/α interface to "feed" the austenite formation as shown in Fig. 1. This leads to very slow migration of the γ/α interface and hence small austenite particles are formed at the ferrite boundaries, as shown in Fig. 5. This result is consistent with the measured kinetics related to the austenite nucleation and growth on ferrite–ferrite grain boundaries by 3-D X-ray diffraction microscopy conducted at the level of individual grains [20].

Although the small-sized austenitic particles that form at the ferrite grain boundaries contribute only little to the overall volume fraction of austenite, it profoundly affects the microstructure evolution of the recrystallizing ferrite:

1. The presence of large population of α_R/α_R boundaries after recrystallization favors austenite nucleation at these sites. However, the appearance of the small-sized austenitic particles will impede grain coarsening within the recrystallized ferrite by pinning the grain boundaries and hence stabilize the microstructures. This effect promotes microstructure refinement of the DP steel processed by intercritical annealing.
2. At the moving α_R/α_{NR} boundaries, however, the recrystallization front is suffering pinning due to appearance of the fine austenitic particles. This effect might slow down the recrystallization rate slightly. Yet the moving interface can easily escape across these small particles owing to insufficient pinning, particularly at the early stage of the recrystallization. These particles of grain-boundary-nucleated austenite are then changed to be intragranularly located, as shown in Fig. 5c. In experimental observations, intragranular austenitic particles were usually considered to be associated with the presence of carbides within the ferrite matrix prior to transformation that can stimulate austenite nucleation and support the growth by the surplus of carbon [9]. Obviously, current simulation reveals another reasonable explanation about the mechanism of their formation from the perspective of interaction between recrystallization and phase transformation.
3. At the α_{NR}/α_{NR} boundaries, the situation becomes more complex since recrystallization and phase transformation both are preferentially nucleated at these sites. This indicates that the austenite nucleation occurs in competition with the nucleation of ferrite recrystallization at the α_{NR}/α_{NR} boundaries. However, the extensive nucleation of the fine austenite precipitates will inversely stabilize the deformation structure and thus hinder the ferrite recrystallization. It will influence the subsequent development of the microstructure in following annealing steps.

It should be pointed out that the discussions so far are made in two dimensions based on the 2-D simulations. This might give rise to potential limitations implied by the 2-D nature of the simulation. In the current simulation, the simulated domain is selected within the 2-D cut parallel with the rolling direction, which hence contains more alignment-like deformation structures of ferrite grains and pearlite colonies in the considered section compared to that within other 2-D sections, e.g. the cross-section of the 3-D microstructure. This indeed implies an exaggerated effect of topological restrictions on ferrite recrystallization derived from the initial banded microstructure, which thus leads to a much slower recrystallization rate compared to 3-D simulations. In addition, the pinning effect on the recrystallization exerted by the formation of the small-sized austenite particles in 2-D simulation is actually larger than that in three dimensions [44]. Consequently, the intragranular austenitic particles as shown in Fig. 5 occur less frequently than those in the 3-D simulation such that they may be found located mainly at the grain boundaries in current 2-D results. This might also render the 2-D recrystallization kinetics slightly different from corresponding 3-D results. Despite the limitations, however, current 2-D simulation presents a successful microstructural description of the interaction between recrystallization and phase transformation. We can find that the interaction between ferrite recrystallization and austenite formation does affect not only the transformation kinetics but also the morphology and spatial distribution of austenite.

Fig. 6 shows the resultant microstructure as the result of concurrent ferrite recrystallization and austenitic transformation in carbon steels derived from both the micrographs [11] and the simulations. A detailed comparison among the various microstructural constituents is made in Fig. 6c. It can be seen that the simulated phase arrangement and

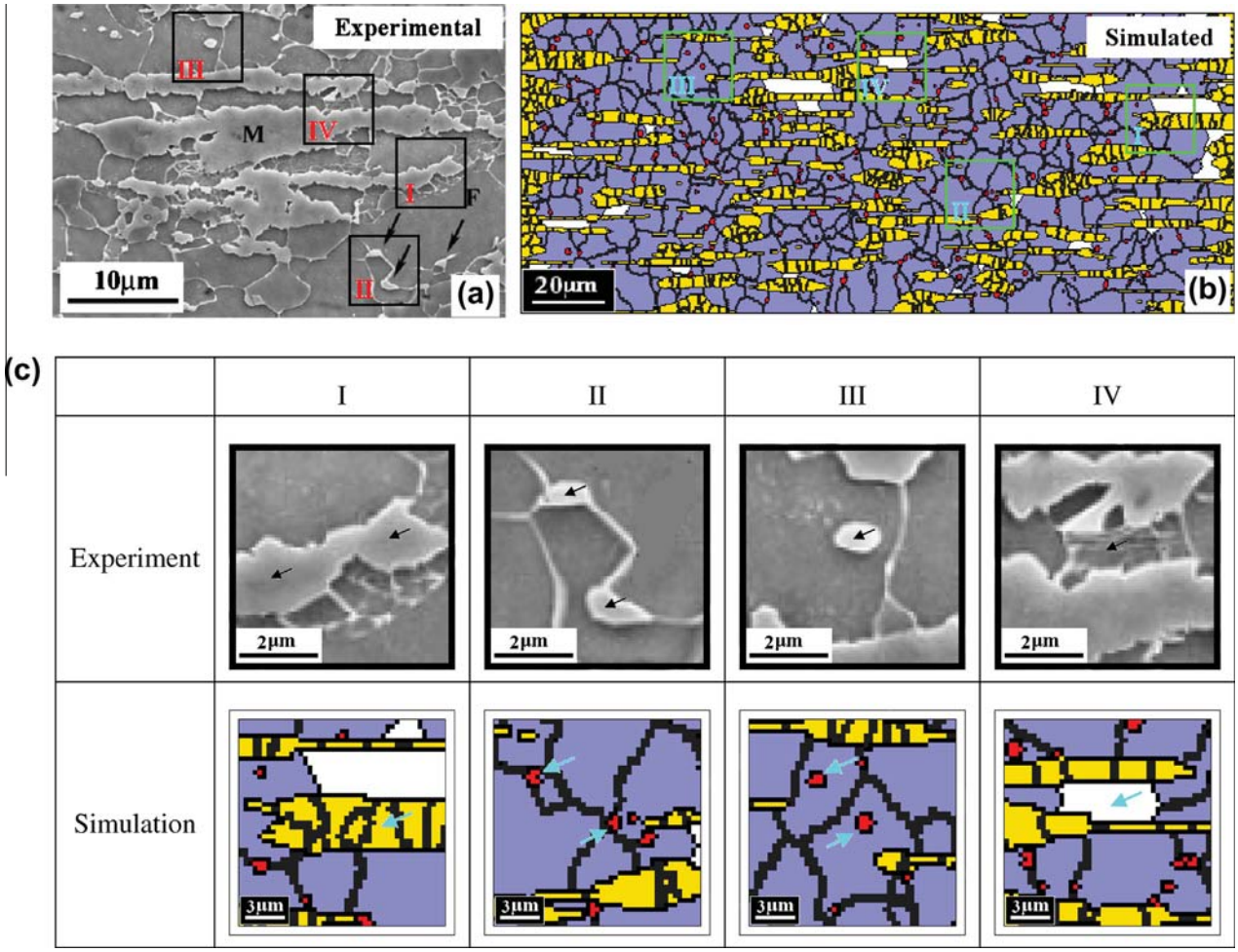

Fig. 6. Comparison of the resultant microstructure between the micrographs (a) and the simulations (b) as a result of competitive ferrite recrystallization and austenitic transformation in carbon steels. Details of the various microstructural constituents are shown in (c) with (I) the austenitic islands formed from prior pearlitic regions; (II) the austenitic patches located at the ferrite grain boundaries; (III) intragranular austenite grains; and (IV) the unrecrystallized ferrite zone. In the simulated microstructure, the yellow areas are the pearlite-nucleated austenite and the small-sized red patches are the grain-boundary-nucleated austenite. The blue regions indicate the recrystallized ferrite and the white zones are the unrecrystallized ferrite. The black lines in the figures indicate grain boundaries. The micrograph result is taken from Ref. [11]. (For interpretation of the references to color in this figure legend, the reader is referred to the web version of this article.)

the grain structure resemble the micrographic results very well in both the grain morphology and their spatial distribution. The present CA modeling can reproduce the recrystallization and the phase transformation satisfactorily and also match the experimental results well.

5.2. Effect of the annealing temperature

Further understanding on the interaction between recrystallization and phase transformation can also be made by examining the microstructure changes for different intercritical temperatures. Fig. 7a and b shows the simulated transformation kinetics of ferrite recrystallization and austenite formation, respectively, at different annealing temperatures. We observe that recrystallization and phase transformation are both promoted significantly with the increase of the annealing temperature.

As a diffusion-controlled process, austenite formation should be easier at higher temperature in the intercritical regime. Firstly, the carbon solubility in austenite reduces with the temperature increase. Therefore, less carbon is required to form austenite at the transforming γ/α interface. The phase transformation is more facilitated and produces larger amounts of austenite, as shown in Fig. 7b. Secondly, higher annealing temperature leads to higher diffusivity of carbon. Thus, transfer of carbon within the pearlite-nucleated austenite or across the ferrite zones becomes easier to "feed" carbon for austenite formation at the γ/α interfaces. This will evidently accelerate the phase transformation. Thirdly, both the mobility of the moving interface and the chemical driving force for the phase transformation are increased, which also leads to a higher transformation rate.

As a thermally activated process, ferrite recrystallization is also enhanced upon temperature increase. Its kinetics is

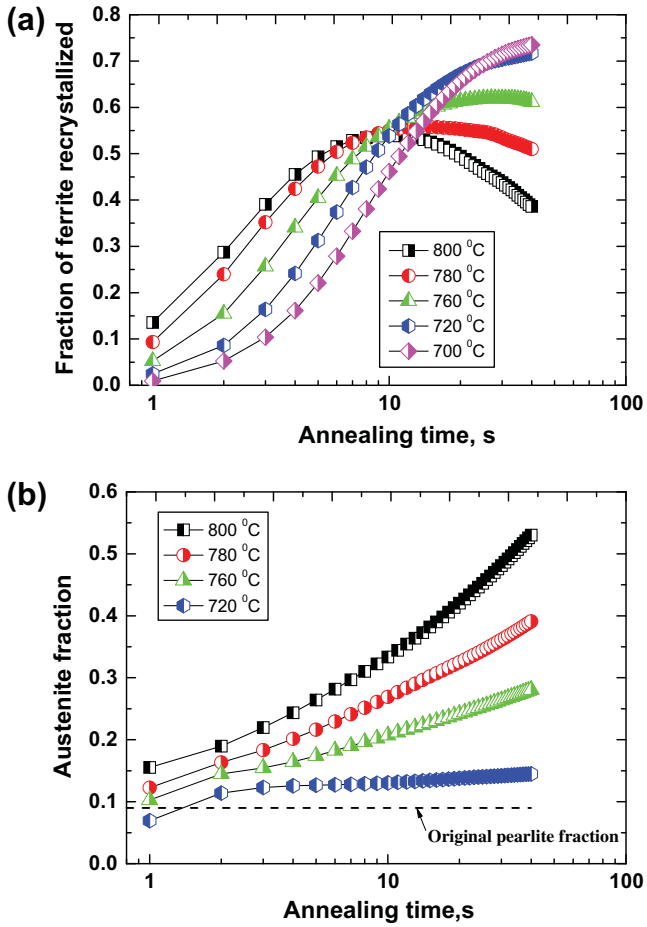

Fig. 7. Simulated transformation kinetics of ferrite recrystallization (a) and austenite formation (b) during isothermal holding at various annealing temperatures.

closely correlated with the progress in phase transformation, as revealed by Fig. 7a. At the ferritic temperature of 700 °C, without occurrence of phase transformation, the recrystallized fraction increases gradually, following a typical sigmoidal curve [29]. Within the intercritical temperature range, recrystallization proceeds much faster with increasing annealing temperature. The recrystallized fraction drops significantly at the late stage of the phase transformation. This declining trend becomes more obvious at higher intercritical annealing temperatures. At the intercritical temperature of 800 °C, a distinct fraction peak appears in the recrystallization kinetics. This microstructural result can be applied to rationalize the observed property variation of the studied steel in more detail.

In a previous study, Peranio et al. [45] analyzed the competition between ferrite recrystallization and phase transformation in a cold-rolled DP steel by performing a series of hardness measurements on differently annealed samples. For annealed DP steels, the softening effect caused by ferrite recrystallization is responsible for the hardness reduction, whereas hardness increase is correlated with the ongoing austenite formation during annealing as it turns into martensite after quenching. Therefore, the

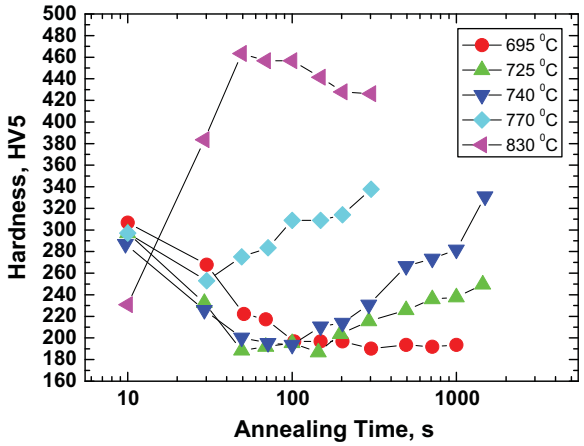

Fig. 8. Experimentally observed hardness values as a function of the annealing time, measured in cold-rolled DP steel sheets at various ferritic or, respectively, intercritical annealing temperatures [45].

hardness of the steel after quenching is a consequence of the dynamic balance between ferrite recrystallization softening and phase transformation hardening, as shown in Fig. 8. However, the hardness measurement alone is an integral measure and does not include any topological information on the development of the different microstructural constituents, be it the recrystallized ferrite dispersion or the transformed austenite or, respectively, martensite fraction. The current simulation can provide this information, and hence enables a closer inspection of the kinetic and morphological interactions between the two metallurgical processes on a microscopic level as well as their mechanical consequences.

In Fig. 8, we observe that at the ferritic temperature of 695 °C the hardness decreases gradually with annealing time and then remains constant during the subsequent transformation. This course reveals the individual softening process associated with ferrite recrystallization, as shown by the simulation result for 700 °C in Fig. 7. The hardness minimum corresponds to the state where the ferrite recrystallization is completed. When the temperature increases within the lower intercritical temperature range (e.g. see hardness data and microstructures at $T = 725$ °C and 740 °C), the reduction in hardness is faster due to the accelerated ferrite recrystallization. However, in these cases the hardness increases continuously. This is attributed to the ongoing phase transformation, which leads to an increase in the martensite volume fraction after quenching. At the medium intercritical temperature regime (e.g. $T = 770$ °C), the hardness is observed to decrease slowly at the early stage of the transformation. Surprisingly, the hardness drops much more slowly compared to the decline observed at lower temperatures. This is attributed to the fact that in the experiments the ferrite recrystallization accelerates with increasing temperature, as seen in the simulation at 780 °C, whereas the recrystallization softening is gradually compensated by the competing hardening associated with the phase transformation. When the hardening

effect through an increase in the martensite fraction exceeds the ferrite recrystallization softening, the effective hardness rises again before reaching a minimum value. A microstructural example of this interaction can be found in the simulation at 780 °C in Fig. 7. When the temperature increases to a value above the intercritical temperature of 830 °C, ferrite recrystallization and phase transformation are both accelerated significantly. The rapid recrystallization softening leads to a very rapid reduction in hardness. It is observed that the hardness already decreases to 230HV5 after a short annealing time of 10 s. Thereafter, the hardness increases sharply again owing to the rapid austenite formation. The phase transformation proceeds to such an extent that the hardness increases above the value observed after the initial cold rolled sheets. The corresponding microstructural prediction of this process is shown by the simulation results obtained for 800 °C in Fig. 7.

It is clear that the present modeling cannot in all cases exactly reproduce all microstructural features pertaining to a specific set of experimental parameters of the studied DP steel. However, it enables us to reveal and manipulate the details of the competing microstructural mechanisms with the aim to design optimal microstructures. For instance, in the current model, the incubation time both of the recrystallization and for the phase transformation is not taken into account. This might cause a discrepancy between the hardness measurements and the kinetics extracted from the microstructural simulations, especially within the lower intercritical temperature region. With the temperature increasing, however, the incubation time is decreased significantly [45] and the effect of the incubation time becomes negligible.

Fig. 9 shows the simulated microstructure and associated carbon concentration fields in austenite after the isothermal annealing up to 40 s at three different temperatures. In the right-hand-side images, the carbon-depleted areas where the carbon concentration is below 0.01 wt.% indicate the ferrite phase. During the intercritical annealing, the austenite forms preferentially within the isolated pearlite colonies with different sizes and then grows up gradually controlled by the carbon diffusion in austenite. However, the carbon diffusion distance is determined by the grain size of the isolated austenite islands. As a result, carbon concentration variations exist among the different austenite grains due to the inhomogeneous morphology of the microstructure at all three temperatures (Fig. 9). Moreover, significant carbon concentration gradients are still sustained within some large austenite regions. This result indicates that the growth rates of individual austenite grains can substantially differ from each other during transformation.

Fig. 9 reveals further important effects regarding the distribution and morphology of the austenite. At 800 °C the pearlite-nucleated austenite and the grain-boundary-nucleated austenite both prevail significantly compared to that at lower temperatures. Relatively large austenite islands can be observed as well as isolated fine austenite islands that are distributed on the ferrite boundaries, forming a necklace-type arrangement of new grains along the grain boundaries. At lower temperatures, however, the austenite grains that were formed at the ferrite grain boundaries are substantially smaller. Furthermore, the density of these austenite nuclei is also decreased drastically. We find that the formation of pronounced austenite banding is more pronounced at lower temperatures in comparison with the microstructure obtained after higher-temperature annealing. Another result is that at lower annealing temperature, intragranular austenite occurs more frequently than that at higher temperature. This is because the recrystallization occurs so rapidly at higher annealing temperatures that the austenite prefers to nucleate at the ferrite grain boundaries after recrystallization is completed. At lower intercritical temperature, however, the austenite that nucleated within the partially recrystallized structure easily changes to an intragranular mode due to the rapidly expanding recrystallizing ferrite grains that grow around the austenite nuclei. The associated microstructural features are in accordance with this analysis and are also matched by the temperature-dependent hardness evolution.

5.3. Effect of the heating rate

The microstructures and properties arising from annealing processes that involve transformation phenomena strongly depend on the heating rates ($\dot{R}$) employed. This applies also for the competition between phase transformation and recrystallization. To examine the effect of the initial heating rate in more detail, two distinct heating rates of 5 and 50 °C s^{-1} were tested. Fig. 10 compares the temporal evolutions of the overall austenite fraction during the isothermal holding at 760 and 780 °C, respectively, for the two different heating rates. Fig. 11 shows the corresponding resulting microstructures when just heating to the isothermal temperature and after isothermal holding up to 60 s at 760 °C for the two initial heating rates. We observed that both the transformation kinetics and resulting microstructures change profoundly under these different reheating conditions.

In general, at lower heating rates, the recrystallization starts earlier than the austenite transformation [45]. Hence, under these constraints, sufficient time is available for recrystallization to take place during the heating process. Fig. 12 shows the simulated kinetics of ferrite recrystallization upon heating at a rate of 5 °C s^{-1} together with the evolving microstructure. We observe that most of the deformed ferrite matrix has been replaced by equiaxed recrystallized ferrite grains before austenite formation starts. The presence of a large fraction of recrystallized ferrite will facilitate subsequent austenite formation at the ferrite boundaries. The results shown in Fig 11c reveal that the phase transformation has been stimulated both at the ferrite grain boundaries and within the prior pearlitic zones before reaching the soaking temperature. In this scenario,

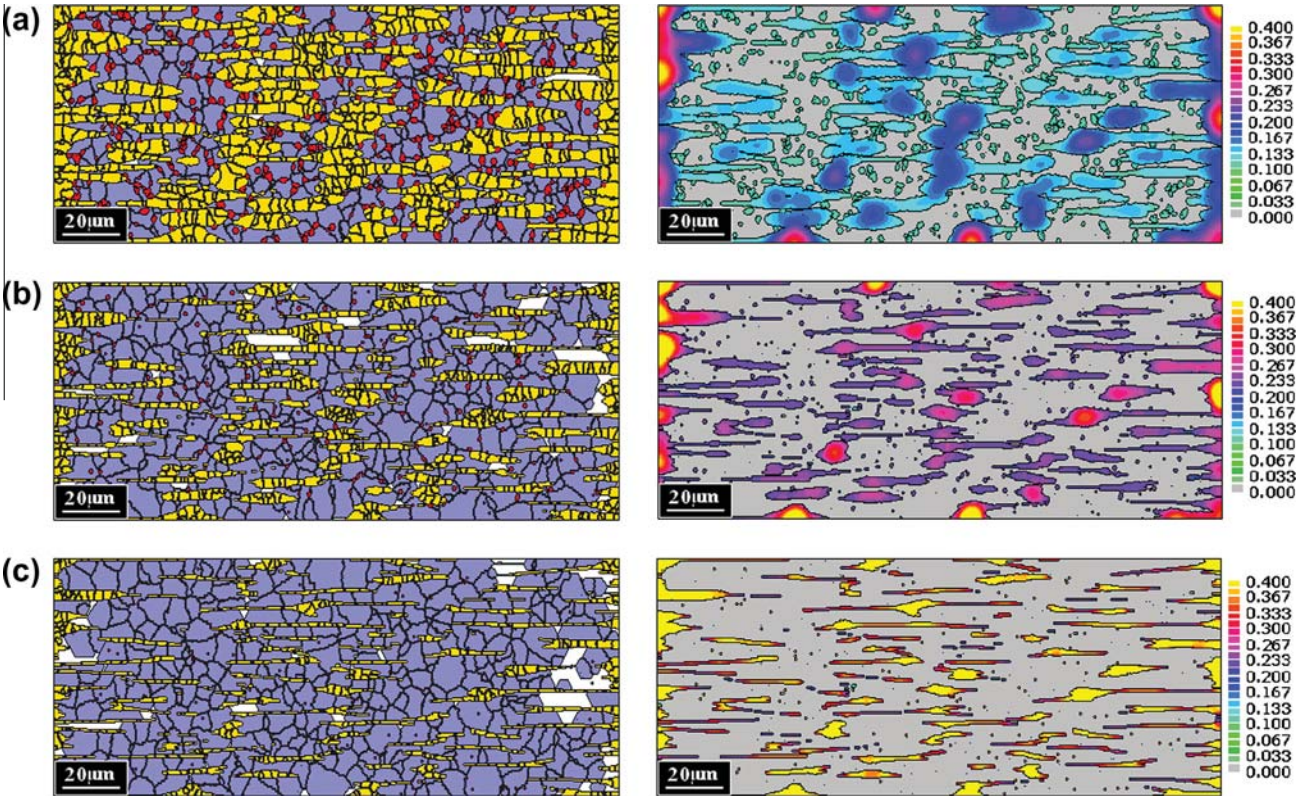

Fig. 9. Simulated microstructure (left) and carbon concentration field (wt.%) in the austenite phase (right) after isothermal holding of 40 s at different soaking temperatures: (a) $T = 800$ °C, (b) $T = 760$ °C; (c) $T = 720$ °C during isothermal intercritical annealing. In the simulated microstructure, the yellow areas are the pearlite-nucleated austenite and the small-sized red patches are the grain-boundary-nucleated austenite. The blue regions indicate recrystallized ferrite and the white zones are unrecrystallized ferrite. The black lines in the figures indicate the grain boundaries. (For interpretation of the references to color in this figure legend, the reader is referred to the web version of this article.)

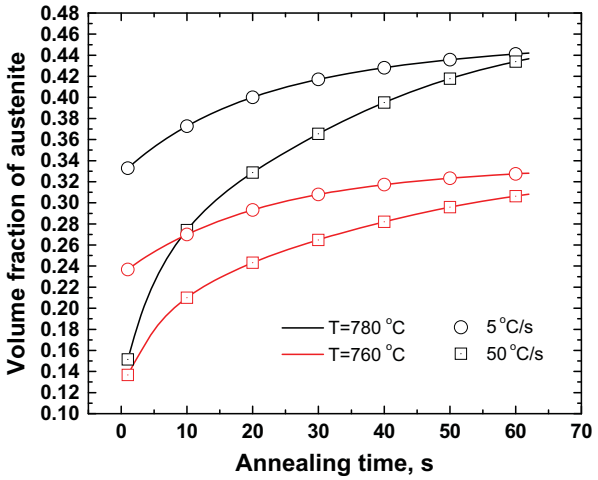

Fig. 10. Effect of initial heating rate on the kinetics of isothermal austenite formation during holding at 780 and 760 °C, respectively.

extensive growth of the boundary-nucleated austenite is promoted with significant competition with the pearlite-nucleated austenite during isothermal holding. As a result, a network of fine and evenly distributed austenite islands is formed along the boundaries for the lower initial heating rate. When the heating rate is increased, both recrystallization and phase transformation are delayed. As shown in Fig. 11a, although the pearlite-to-austenite transformation process is relatively fast, the pearlite does not dissolve completely during heating at the given rate of 50 °C s^{-1}. Recrystallization and phase transformation then take place simultaneously during the subsequent isothermal holding. Compared with the case of the lower heating rate, austenite nucleation at the ferrite boundaries is strongly delayed. Associated with this is the preferential growth of the pearlite-nucleated austenite without significant competition from the boundary-nucleated austenite. Conversely, growth of the grain-boundary-nucleated austenite is hampered. As a result, at higher heating rates a complex microstructure is formed that is composed of a pronounced banded structure containing smaller austenite patches. This simulation result is consistent with the experimental findings that a morphological transition occurs from randomly distributed to a more banded structure of austenite when increasing the heating rate [11].

Another result of interest is that although significant differences exist in the austenite volume fraction at the initial stage of the isothermal annealing for various initial heating rates, these differences should eventually disappear; i.e. given enough soaking time, the steel will reach the equilibrium austenitic fraction at the given intercritical

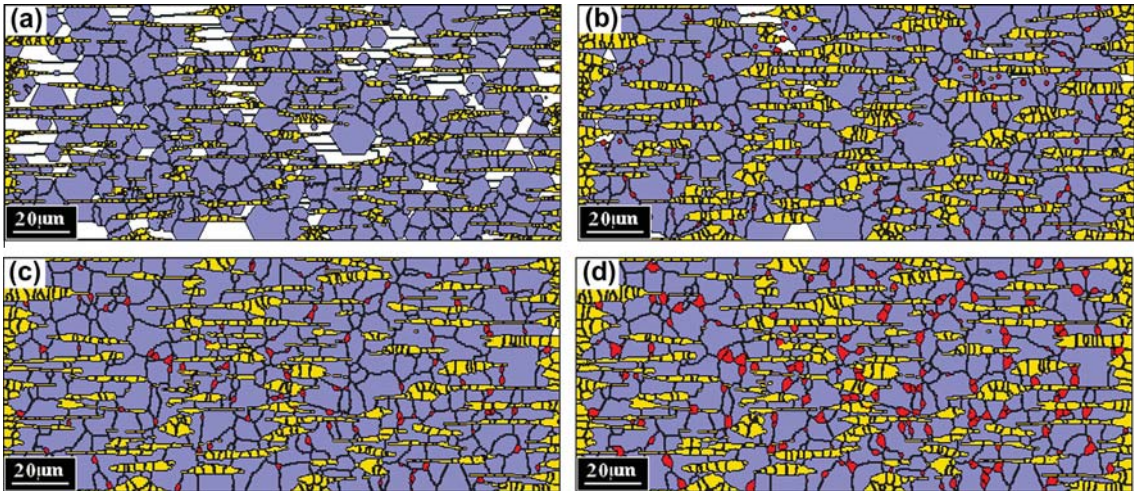

Fig. 11. Simulated microstructures both at the beginning of isothermal holding (a, c) and after isothermal holding of 60 s (b, d) at 760 °C with initial heating rates of 50 and 5 °C s^{-1}, respectively: (a) $t = 0$ s, $\dot{R} = 50$ °C s^{-1}; (b) $t = 60$ s, $\dot{R} = 50$ °C s^{-1}; (c) $t = 0$ s, $\dot{R} = 5$ °C s^{-1}; (d) $t = 60$ s, $\dot{R} = 5$ °C s^{-1}. In the microstructures depicted, the yellow areas represent the pearlite-nucleated austenite and the small-sized red patches are the grain-boundary-nucleated austenite grains. The blue regions indicate the recrystallized ferrite and the white zones indicate the unrecrystallized ferrite. The dark gray regions are the pearlite colonies. The black lines in the figures indicate grain boundaries. (For interpretation of the references to color in this figure legend, the reader is referred to the web version of this article.)

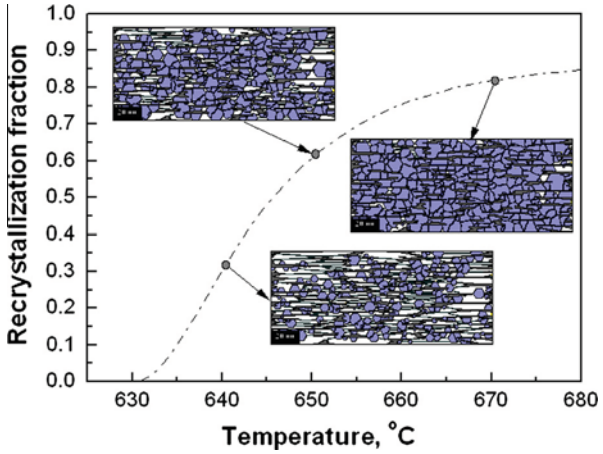

Fig. 12. Simulated kinetics of ferrite recrystallization together with the corresponding microstructure changes during continuous heating at a rate of 5 °C s^{-1}. In the microstructures, the blue regions indicate the recrystallized ferrite and the white zones are unrecrystallized ferrite. The dark gray regions are the pearlite colonies. The black lines in the figures indicate grain boundaries. (For interpretation of the references to color in this figure legend, the reader is referred to the web version of this article.)

temperature, as seen in Fig. 10. The difference in austenite fractions is vanishing much faster at higher annealing temperatures. This is due to the accelerated transformation when increasing the annealing temperature.

However, it should be pointed out that in this simulation, the effect of the stored deformation energy as an additional portion to the driving force for phase transformation is not considered. Therefore, acceleration of the austenite formation due to the non- or partial recrystallization, i.e. the preferred nucleation and faster austenite growth in non-recrystallized microstructures [46] cannot be simulated by this model. This thus might cause discrepancies of current simulation results with the experimental findings by several other authors [10,47] in the effect of the heating rate on the kinetics of austenite formation during the reheating process. For example, Andrade-Carozzo and Jacques [47] found a considerable increase in martensite volume fraction with increasing heating rate and they attributed these microstructural changes to the preservation of the defect structure in the non-recrystallized ferrite owing to the rapid reheating and hence increasing the austenite nucleation rate. Despite the above-mentioned limitation, however, the observed morphological transitions as functions of heating rates are well reproduced by the current simulations.

It should also be pointed out that in CA models the grid size is usually of the order of 0.1 μm, which is too coarse to describe individual lamellae of ferrite and cementite in pearlite. Therefore, spheroidization and dissolution of cementite lamellae in pearlite colonies cannot be involved. Thus, the pearlite has to be treated as an effective phase in the current approach. Under these constraints, the effect of cementite spheroidization and dissolution on both austenite formation and ferrite recrystallization, especially from broken and scattered cementite fragments, cannot be simulated. Consequently, further improved CA model concepts, e.g. with a more refined grid size, is required to capture also these more subtle and fine scaled microstructural characteristics during intercritical austenite formation in ferrite–pearlite structures. This next step would require separate descriptions of cementite dissolution and the possible austenite formation at the ferrite–cementite interfaces, together with a careful introduction of the initial spatial distributions of the lamellar ferrite–cementite aggregates in the starting microstructure for simulation as presented in Refs. [42,48].

6. Conclusions

In this work, we develop and use a modified 2-D CA model to investigate concurrent ferrite recrystallization and austenitic transformation during intercritical annealing of cold-rolled DP steels. This simulation provides insight into the microstructural phenomena that result from the interaction of primary recrystallization and phase transformation. The simulation shows that the interaction between ferrite recrystallization and austenite formation affects not only the transformation kinetics but also the morphology and spatial distribution of austenite.

The results show that ferrite recrystallization and phase transformation are both promoted significantly with an increase in annealing temperature. Both phenomena are kinetically closely connected. From that we can interpret the experimentally observed temperature-dependent hardness data and their dependence on the two metallurgical processes. Increasing the annealing temperature is found to be favorable for the formation of austenite necklace structures along the grain boundaries.

The results also show that increasing the heating rates produces a variety of initial microstructures ranging from fully recrystallized to partially recrystallized structures prior to austenite formation, which affects the subsequent austenite distribution significantly. We observed that a morphology occurs from randomly distributed to a banded structure of austenite when increasing the initial heating rate. This morphology trend is consistent with experimental findings.

Acknowledgement

C.W.Z. gratefully acknowledges the financial support from the Alexander von Humboldt Foundation.

References

[1] Rocha RO, Melo TMF, Pereloma EV, Santos DB. Mater Sci Eng A 2005;391A:296.
[2] Bleck W, Frehn A, Ohlert J. In: Niobium science and technology: proceedings of the international symposium on niobium, Orlando, FL; 2001. p. 727.
[3] Bhattacharya D. In: Joint international conference of HSLA steels and ISUGS proceedings, Sanya; 2005. p. 70.
[4] Speich GR, Demarest VA, Miller RL. Metall Trans A 1981;12A:1419.
[5] Kim S, Lee S. Metall Mater Trans A 2000;31A:1753.
[6] Nakajima K, Urabe T, Hosoya Y, Kamiishi S, Miyata T, Takeda N. ISIJ Int 2001;41:298.
[7] Rashid MS. In: Davenport AT, editor. Formable HSLA and dual-phase steels. New York: TME/AIME; 1979. p. 1.
[8] Speich GR, Miller RL, Kot RA, Morris JW, editors. Structure and properties of dual-phase steels. New York: TME/AIME; 1979. p. 145.
[9] Yang DZ, Brown EL, Matlock DK, Krauss G. Metall Trans A 1985;16A:1385.
[10] Huang J, Poole WJ, Militzer M. Metall Mater Trans A 2004;35A:3363.
[11] Azizi-Alizamini H, Militzer M, Poole WJ. Metall Mater Trans A 2011;42A:1544.
[12] Raabe D. Philos Mag A 1999;79A:2339.
[13] Militzer M. Curr Opin Solid State Mater Sci 2011;15:106.
[14] Xiao N, Chen Y, Li DZ. Sci China – Technol Sci 2012;55:341.
[15] Rudnizki J, Böttger B, Prahl U, Bleck W. Metall Mater Trans A 2011;42A:2516.
[16] Bos C, Mecozzi MG, Sietsma J. Comput Mater Sci 2010;48:692.
[17] Bos C, Mecozzi MG, Hanlon DN, Aarnts MP, Sietsma J. Metall Mater Trans A 2011;42A:3602.
[18] Okuda K, Yoshida H, Nagataki Y, Tananka Y, Rollett AD. Mater Sci Forum 2007;558–559:1145.
[19] Savran VI, Van Leeuwen Y, Hanlon DN, Kwakernaak C, Sloof WG, Sietsma J. Metall Mater Trans A 2007;38A:946.
[20] Savran VI, Offerman SE, Sietsma J. Metall Mater Trans A 2010;41A:583.
[21] Krielaart GP, Sietsma J, van der Zwaang S. Mater Sci Eng A 1997;237A:216.
[22] Christian JW. The theory of transformations in metals and alloys. Oxford: Pergamon; 2002.
[23] Loginova I, Odqvist J, Amberg G, Ågren J. Acta Mater 2003;51:1327.
[24] Sietsma J, van der Zwaag S. Acta Mater 2004;52:4143.
[25] Bos C, Sietsma J. Scripta Mater 2007;57:1085.
[26] Thermo-Calc Software. <http://www.thermocalc.se/>.
[27] Umemoto M, Guo ZH, Tamura I. Mater Sci Technol 1987;3:249.
[28] Song XY, Rettenmayr M, Müller C, Exner HE. Metall Mater Trans A 2001;32A:2199.
[29] Humphreys FJ, Hatherly M. Recrystallization and related annealing phenomena. 2nd ed. Oxford: Elsevier; 2004.
[30] Raabe D, Hantcherli L. Comput Mater Sci 2005;34:299.
[31] Song X, Rettenmayr M. Mater Sci Eng A 2002;332A:153.
[32] Zheng CW, Xiao NM, Hao LH, Li DZ, Li YY. Acta Mater 2009;57:2956.
[33] Zheng CW, Xiao NM, Li DZ, Li YY. Comput Mater Sci 2008;44:507.
[34] Zener C. Tans AIME 1949;175:15.
[35] Davies CHJ. Scripta Mater 1997;36:35.
[36] Burke JE, Turnbull D. Prog Metal Phys 1952;3:220.
[37] Kremeyer K. J Comput Phys 1998;142:243.
[38] Lan YJ, Xiao NM, Li DZ, Li YY. Acta Mater 2005;53:991.
[39] Zheng C, Xiao N, Li D, Li Y. Comput Mater Sci 2009;45:568.
[40] Thiessen RG, Sietsma J, Palmer TA, Elmer JW, Richardson IM. Acta Mater 2007;55:601.
[41] Offerman SE, van Dijk NH, Sietsma J, Grigull S, Lauridsen EM, Margulies L, et al. Science 2002;298:1003.
[42] Azizi-Alizamini H, Militzer M. Int J Mater Sci Res 2010;101:4.
[43] Pezzee CF, Dunand DC. Acta Metall Mater 1994;42:1509.
[44] Moelans N, Blanpain B, Wollants P. Acta Mater 2005;53:1771.
[45] Peranio N, Li YJ, Roters F, Raabe D. Mater Sci Eng A 2010;527A:4161.
[46] Kulakov M, Poole WJ, Militzer M. Metall Mater Trans A 2013. http://dx.doi.org/10.1007/s11661-013-1721-z.
[47] Andrade-Carozzo V, Jacques PJ. Mater Sci Forum 2007;539–543:4649.
[48] Militzer M, Azizi-Alizamini H. Solid State Phenom 2011;172–174:1050.